Reconstruction and visualization of 3D wind fields from satellite image sequences

Patrick Héas[1], Karl Krissian[2], Etienne Mémin[1], André Szantai[3]
[1]INRIA-IRISA, Rennes, France
[2]University of Gran Canarias, Las Palmas, Spain
[3]Laboratoire de Météorologie dynamique, Paris, France

Abstract

In this paper, we address the problem of estimating and visualizing 3D atmospheric motion using top of cloud pressure image sequences. The reconstruction of 3D fluid motion from a monocular sequence of image observations is a very challenging problem for which no solution exists in the literature. Based on a physically sound vertical decomposition of the atmosphere into layers of different pressure interval, we propose here a dense motion estimator dedicated to the extraction of three-dimensional wind fields characterizing the dynamics of a layered atmosphere. Wind estimation is performed using a multi-layer model describing a stack of dynamic horizontal layers, interacting at their boundaries via vertical winds. Furthermore, a 3D graphical interface is proposed to visualize the horizontal and vertical components of the displacement of each layer. The wind fields are displayed in a physical 3D coordinate system. This system is deduced from pixel coordinates and altitudes estimated from the top of cloud temperature images. Smooth surfaces defining layer vertical boundaries are reconstructed through an altitude extrapolation scheme. An evaluation of the system is performed with Météosat image sequences of top of cloud pressure.

1 Introduction

Geophysical motion analysis by image sequence is a crucial issue for numerous scientific domains involved in the study of climate change, weather forecasting, climate prediction or biosphere analysis. The use of surface station, balloon, and more recently in-flight aircraft measurements and low resolution satellite images has improved the estimation of wind fields and has been a subsequent step for a better understanding of meteorological phenomena. However, the network's temporal and spatial resolutions may be insufficient for the analysis of mesoscale dynamics. Recently, in an effort to avoid these limitations, satellites sensors have been designed to provide image sequences characterized by finer spatial and temporal resolutions. Nevertheless, the analysis of motion remains particularly challenging due to the complexity of atmospheric dynamics at such scales.

Standard techniques from Computer Vision, originally designed for bi-dimensional quasi-rigid motions with stable salient features, appear to be not well adapted [6] [8]. The design of techniques dedicated to fluid flow has been a step forward, towards the constitution of reliable methods to extract characteristic features of flows [2]. However, for geophysical applications, existing fluid-dedicated methods are all limited to horizontal velocity estimation and neglect vertical motion. All these methods are obviously not adapted to the extraction of 3D measurements but also do not take into account accurately luminance variations due to 3D motions. Such effects are occasionally important at small scales and should be incorporated in the motion estimation method. Moreover, in order to analyze and understand the underlying 3D dynamical phenomena, dedicated visualization tools may be helpful for the meteorology community.

2 Related works on wind estimation

The problem of wind field recovery consists in estimating the 3D atmospheric motion denoted by $\mathbf{V}(\mathbf{s},t)$ from a 2D image sequence $I(\mathbf{s},t)$, where $(\mathbf{s},t)$ denote the pixel and time coordinates. This problem is a complex one, for which we have only access to projected information on clouds position and spectral signatures provided by satellite observation channels. To avoid the three-dimensional wind field reconstruction problem, all developed methods have relied on the assumption of negligible vertical winds and focused on the estimation of a global apparent horizontal winds related to top of clouds of different heights.

The estimation of the apparent motion $\mathbf{v}(\mathbf{s},t)$ as perceived through image intensity variations (the so-called optical-flow) relies principally on the temporal conservation of some invariants. The most common invariant used is the brightness constancy assumption. This assumption leads to the well known Optical-Flow Constraint (OFC) equation

$$\mathbf{v}\cdot\nabla I(\mathbf{s},t)+I_t(\mathbf{s},t)=0. \tag{1}$$

An important remark is that for image sequences showing evolving atmospheric phenomena, the brightness consistency assumption does not allow to model temporal distortions of luminance patterns caused by 3D flow transportation. In spite of that, most estimation methods used in the meteorology community still rely on this crude assumption [7]. In the case of transmittance imagery, the Integrated Continuity Equation (ICE) provides a valid invariant assumption for compressible flows [3] under the assumption that the temporal derivatives of the integration boundaries compensate the normal flows. This ICE model reads :

$$\Big(\int\rho dz\Big)_t+\mathbf{v}.\boldsymbol{\nabla}\Big(\int\rho dz\Big)+\Big(\int\rho dz\Big)\mathrm{div}\mathbf{v}=0, \tag{2}$$

where ρ and $\mathbf{v}$ denote the fluid density and the density averaged horizontal motion field along the vertical axis. Unlike the OFC, such models can compensates mass departures observed in the image plan by associating two-dimensional divergence to brightness variations. But, for the case of satellite infra-red imagery, the assumption that $I\propto\int\rho dz$ is flawed. Moreover, note that although the assumed boundary condition is valid for incompressible flows, it is not realistic for compressible atmospheric flows observed at a kilometer order scale. However, based on experiments, authors proposed to apply directly this model to the image observations [2].

The formulations of Eq.1 and Eq.2 can not be used alone, as they provide only one equation for two unknowns at each spatio-temporal locations $(\mathbf{s},t)$, with therefore a one dimensional family of solutions in general. In order to remove this ambiguity and improve the robustness of the estimation, the most common assumption consists in enforcing a spatial local coherence. The latter can explicitly be expressed as a regularity prior in a globalized smoothing scheme. Within this scheme, spatial dependencies are modeled on the complete image domain and thus robustness to noise and low contrasted observations is enhanced. More precisely, the motion estimation problem is defined as the global minimization of an energy functional composed of two components :

$$J(\mathbf{v},I)=J_d(\mathbf{v},I)+\alpha J_r(\mathbf{v}). \tag{3}$$

The first component $J_d(\mathbf{v},I)$ called the data term, expresses the constraint linking unknowns to observations while the second component $J_r(\mathbf{v})$, called the regularization term, enforces the solution to follow some smoothness properties. In the previous expression, $\alpha>0$ denotes a parameter controlling the balance between the smoothness and the global adequacy to the observation model. In this framework, Horn and Schunck [6] first introduced a data term related to the OFC equation and a first-order regularization of the two spatial components u and v of velocity field $\mathbf{v}$. In the case of transmittance imagery of fluid flows, $I=\int\rho dz$, and using the previously defined ICE model (Eq.2) leads to the functional :

$$J_d(\mathbf{v},I)=\int_\Omega\left(I_t(\mathbf{s})+\mathbf{v}(\mathbf{s})\cdot\boldsymbol{\nabla}I(\mathbf{s})+I(\mathbf{s})\mathrm{div}\mathbf{v}(\mathbf{s})\right)^2d\mathbf{s}, \tag{4}$$

where Ω denotes the image domain. Moreover, it can be demonstrated that a first order regularization is not adapted as it favors the estimation of velocity fields with low divergence and low vorticity. A second

order regularization on the vorticity and the divergence of the defined motion field can advantageously be considered as proposed in [2][10]:

$$J_r(\mathbf{v}) = \int_\Omega \parallel \boldsymbol{\nabla} curl\mathbf{v}(\mathbf{s}) \parallel^2 + \parallel \boldsymbol{\nabla} \mathrm{div}\mathbf{v}(\mathbf{s}) \parallel^2 d\mathbf{s}. \tag{5}$$

Instead of relying on a $\boldsymbol{L}^2$ norm, robust penalty function ϕ_d may be introduced in the data term for attenuating the effect of observations deviating significantly from the ICE constraint [1]. Similarly, a robust penalty function ϕ_r can be used if one wants to handle implicitly the spatial discontinuities of the vorticity and divergence maps. In the image plan, these discontinuities are nevertheless difficult to relate to abrupt variations of clouds height. Moreover, the robust approach does not allow points of unconnected regions, which belong to a same layer, to interact during the motion estimation process.

3 Estimation of 3D winds

3.1 Integrated Continuity Equation for 3D winds

Interesting models for 3D compressible atmospheric motion observed through image sequences may be derived by integrating the 3D continuity equation expressed in the isobaric coordinate system (x, y, p). In comparison to standard altimetric coordinates, isobaric coordinates are advantageous : they enable to handle in a simple manner the compressibility of atmospheric flows while dealing directly with pressure quantities, which will be used as observations in this paper. In this coordinate system, the pressure function p acts as a vertical coordinate. Let us denote the horizontal wind components by $\mathbf{v} = (u, v)$ and the vertical wind in isobaric coordinates by ω. The 3D continuity equation reads [5] :

$$-\frac{\partial \omega}{\partial p} = \left(\frac{\partial u}{\partial x} + \frac{\partial v}{\partial y}\right)_p. \tag{6}$$

By defining now two altimetric surfaces s^k and s^{k+1} with $p(s^k) > p(s^{k+1})$ related to a pressure difference function h^k and a pressure-average horizontal wind field $\mathbf{v}^k$

$$\begin{aligned} h^k &= p(s^k) - p(s^{k+1}) \\ \mathbf{v}^k &= \frac{1}{h^k} \int_{p(s^{k+1})}^{p(s^k)} \mathbf{v} dp, \end{aligned} \tag{7}$$

it can be demonstrated that the vertical integration of Eq.6 in the altimetric interval $[s^k, s^{k+1}]$ yields under certain conditions to the following 3D-ICE model:

$$g\rho(s^k)\mathrm{w}(s^k) - g\rho(s^{k+1})\mathrm{w}(s^{k+1}) = \frac{dh^k}{dt} + h^k \mathrm{div}(\mathbf{v}^k), \tag{8}$$

where g and w denote the gravity constant and the vertical wind in the standard altimetric coordinate system (x, y, z). Note that this model appears to be a generalization of the so called *kinematic method* applied in meteorology for the recovery of vertical motion [5]. Indeed, by neglecting the first term on the right hand side of Eq.8, vertical motion can be expressed as :

$$\mathrm{w}(s^{k+1}) = \frac{\rho(s^k)\mathrm{w}(s^k)}{\rho(s^{k+1})} - \frac{h^k}{g\rho(s^{k+1})}\mathrm{div}(\mathbf{v}^k), \tag{9}$$

which corresponds exactly to the *kinematic* estimate. Note also that the ICE model (Eq.2) can be recovered when vertical motion is neglected and for an atmosphere in hydrostatic equilibrium ($\delta p = -g \int \rho dz$). On the right side of the 3D-ICE, vertical motion w appears only on the integration boundaries, while on the left side, pressure-average horizontal motion $\mathbf{v}^k$ appears within a standard optical flow expression compensated by a divergence correcting term. Thus, for pressure difference observations on layer boundaries, the 3D-ICE constitutes a possible 3D estimation model.

3.2 Layer decomposition

The layering of atmospheric flow in the troposphere is valid in the limit of horizontal scales much greater than the vertical scale height, thus roughly for horizontal scales greater than 100 km. It is thus impossible to guarantee to truly characterize a layered atmosphere with a local analysis performed in the vicinity of a pixel characterizing a kilometer order scale. Nevertheless, one can still decompose the 3D space into elements of variable thickness, where only sufficiently thin regions of such elements may really correspond to common layers. Analysis based on such a decomposition presents the main advantage of operating at different atmospheric pressure ranges and avoids the mix of heterogeneous observations.

Let us present the 3D space decomposition that we chose for the definition of the layers. The k-th layer corresponds to the volume lying in between an upper surface s^{k+1} and a lower surface s^k. These surfaces s^j are defined by the height of top of clouds belonging to the j-th layer. They are thus defined only in areas where there exists clouds belonging to the j-th layer, and remains undefined elsewhere. The membership of top of clouds to the different layers is determined by cloud classification maps. Such classifications which are based on thresholds of top of cloud pressure, are routinely provided by the EUMETSAT consortium, the European agency which supplies the METEOSAT satellite data.

3.3 Sparse pressure difference observations

Top of cloud pressure images are also routinely provided by the EUMETSAT consortium. They are derived from a radiative transfer model using ancillary data obtained by analysis or short term forecasts [9].

We denote by C^k the class corresponding to the k-th layer. Note that the top of cloud pressure image denoted by $p_{\bigcup}$ is composed of segments of top of cloud pressure functions $p(s^{k+1})$ related to the different layers. That is to say : $p_{\bigcup} = \{\bigcup_k p(s^{k+1}, \mathbf{s});\ \mathbf{s} \in C^k\}$. Thus, pressure images of top of clouds are used to constitute sparse pressure maps of the layer upper boundaries $p(s^{k+1})$. As in satellite images, clouds lower boundaries are always occluded, we coarsely approximate the missing pressure observations $p(s^k)$ by an average pressure value $\overline{p}^k$ observed on top of clouds of the layer underneath. Finally, for the k-th layer, we define observations as pressure differences :

$$\overline{p}^k - p_{\bigcup} = \begin{cases} = h^k(\mathbf{s}) & if \quad \mathbf{s} \in C^k \\ \neq h^k(\mathbf{s}) & if \quad \mathbf{s} \in \bar{C}^k, \end{cases} \tag{10}$$

3.4 Layer interacting model

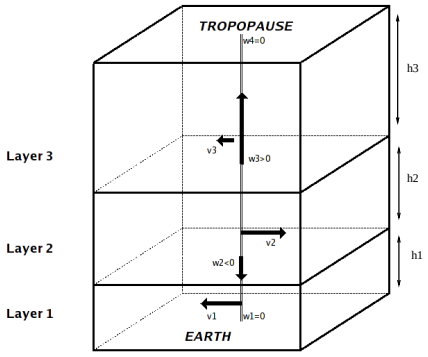

Figure 1: Scheme of three interacting layers defined at a given pixel location. The set of unknowns associated to the corresponding 3D-ICE model is $\{\mathbf{v}^1, w^2, \mathbf{v}^2, w^3, \mathbf{v}^3\}$. For the enhancement of the visual representation, pressure difference h^k have been identified here to altimetric heights.

Eq.8 is thus valid for image observations h^k related to the k-th layer on the spatial sub-domain C^k:

$$\frac{d(h^k)}{dt} + h^k \nabla \cdot \mathbf{v}^k = g(\rho^k \mathrm{w}^k - \rho^{k+1} \mathrm{w}^{k+1}), \tag{11}$$

where for clarity we have simplified notations $\rho(s^k)$ and $w(s^k)$ into ρ^k and w^k. Density maps ρ^k are fixed to a mean density value, which is computed according to the mean pressures $\overline{p}^k$ using the approximation : $\rho^k \approx p_0/(RT_0)(\overline{p}^k/p_0)^{(\gamma R)/g+1}$, where p_0, T_0, γ and R denote physical constants [5].

Integrating in time differential equation 11 along the horizontal trajectories and applying the variation of the constant technique for the second member, we obtain a time-integrated form :

$$\tilde{h}^k e^{\mathrm{div}\mathbf{v}^k} - h^k = g\Delta t \frac{\rho^k \mathrm{w}^k - \rho^{k+1}\mathrm{w}^{k+1}}{\mathrm{div}\mathbf{v}^k}(e^{\mathrm{div}\mathbf{v}^k} - 1), \tag{12}$$

where the motion-compensated image $h^k(\mathbf{s}+\mathbf{v}^k, t+\Delta t)$ has been denoted for convenience by $\tilde{h}^k$ and where Δt denotes the time interval expressed in seconds between two consecutive images.

For the lowest layer, the Earth boundary condition implies : $\mathrm{w}^1 = 0$. Let K denote the index of the highest layer. Another boundary conditions may be given for the highest layer by the reasonable assumption that vertical wind can be neglected at the tropopause which acts like a cover : $\mathrm{w}^{K+1} = 0$. Thus, as the vertical wind present on the upper bound of the k-th layer is identical to the one present on the lower bound of the $(k+1)$-th layer, we have the following two sets of unknowns : $\{\mathbf{v}^k : k \in [1, K]\}$ and $\{\mathrm{w}^k : k \in [2, K]\}$. The vertical wind unknowns act as variables materializing horizontal wind interactions between adjacent layers. Fig.1 schematizes an example of three interacting layers associated to a set of unknowns, according to the 3D-ICE model.

3.5 Dedicated robust estimator

Since outside the class C^k, h^k defined in Eq.10 is not relevant of the k-th layer, we introduce a masking operator to remove unreliable observations by saturation of a robust penalty function ϕ_d. More explicitly, we denote by $\mathbb{I}_{C^k}$ the operator which is identity if pixel belong to the class, and which returns a fixed value out of the range taken by h^k otherwise. Thus, applying this new masking operator in Eq.12, we obtain for the k-th layer the robust data term

$$J_d(\mathbf{v}^k, \mathrm{w}^k, \mathrm{w}^{k+1}, h^k) = \int_\Omega \phi_d\big[\tilde{h}^k(\mathbf{s})\exp\{\mathrm{div}\mathbf{v}^k(\mathbf{s})\} - \mathbb{I}_{C^k}(h^k(\mathbf{s})) + g\Delta t \frac{\rho^k \mathrm{w}^k(\mathbf{s}) - \rho^{k+1}\mathrm{w}^{k+1}(\mathbf{s})}{\mathrm{div}\mathbf{v}^k(\mathbf{s})}(1 - \exp\{\mathrm{div}\mathbf{v}^k(\mathbf{s})\})\big] d\mathbf{s}. \tag{13}$$

A second order div-curl regularizer has been chosen to constrain spatial smoothness of horizontal wind fields. The latter was combined with a first order regularizer enforcing regions of homogeneous vertical winds. Note that we have restricted the regularizer for vertical wind to be a first order one, as 3D divergence and 3D vorticity vectors are inaccessible in a layered model. The regularization term for the k-th layer has been thus defined as

$$J_r(\mathbf{v}^k, \mathrm{w}^k) = \int_\Omega \alpha(\| \nabla curl\mathbf{v}^k(\mathbf{s}) \|^2 + \| \nabla \mathrm{div}\mathbf{v}^k(\mathbf{s}) \|^2) + \beta \| \nabla \mathrm{w}^k(\mathbf{s}) \|^2 d\mathbf{s}, \tag{14}$$

where $\beta > 0$ denotes a positive parameter. A Leclerc M-estimator has been chosen for ϕ_d for its advantageous minimization properties [4]. The masking procedure together with the use of this robust penalty function on the data term allows discarding implicitly the erroneous observations from the estimation process. It is important to outline that, for the k-th layer, the method provides estimates on all point s of the image domain Ω. Areas outside the cloud class C^k correspond to 3D interpolated wind fields.

3.6 Minimization issues

In the proposed optimization scheme, we chose to minimize a discrete linearized version of functionals of Eq. 13 and Eq. 14. Let us denote by z^k the robust weights associated to the semi-quadratic penalty function related to the data term. Minimization is done by alternatively solving large systems for unknowns $\mathbf{v}^k$, w^k and z^k through a multigrid Gauss-Seidel solver. More explicitly, all variables are first initialized to zero. A global optimization procedure is then successively operated at each level of the multiresolution pyramid. This procedure first performs in a multigrid optimization strategy, the minimization with respect to $\mathbf{v}^k$. As variables $\{\mathrm{w}^k\}$ and $\{z^k\}$ are first frozen, this first step can be performed independently for each layer level $k \in [1, K]$. Once the minimum have been reached, in a second step, fixing variables $\{\mathbf{v}^k\}$ and $\{z^k\}$, the same functional is minimized with respect to each $\mathrm{w}^k, k \in [2, K]$. Note that vertical wind w^k is

estimated considering variables related to the layer above the boundary $\{\mathrm{w}^{k+1}, h^k, \tilde{h}^k, \mathbf{v}^k, z^k\}$ and the layer underneath the boundary $\{\mathrm{w}^{k-1}, h^{k-1}, \tilde{h}^{k-1}, \mathbf{v}^{k-1}, z^{k-1}\}$. Finally, in a last step for each pixel locations and for each $k \in [1, K]$, the robust weights z^k are in turn updated while variables $\{\mathbf{v}^k\}$ and $\{\mathrm{w}^k\}$ are kept fixed. The three previous minimization steps are iterated until a global convergence criterion is reached, that is to say until the variation of the estimated solution between two consecutive iterations becomes sufficiently small.

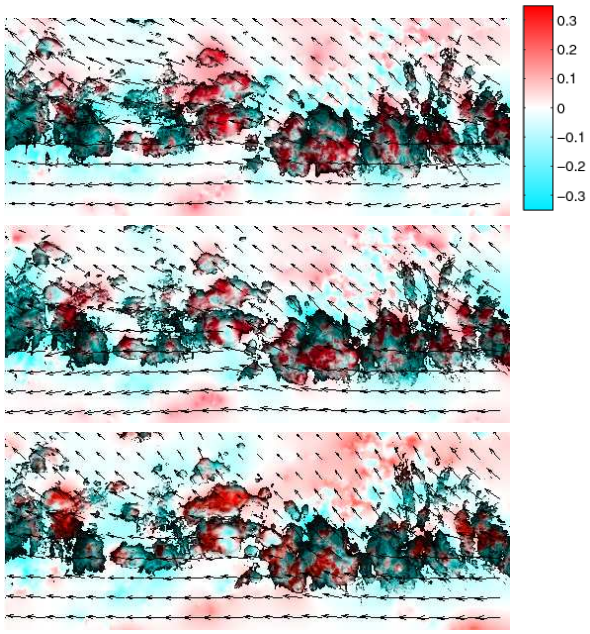

Figure 2: ***Estimation of 3D wind in atmospheric convective systems.*** *Cloud pressure difference images of the highest layer at 3 consecutive times (from top to bottom). Estimated horizontal wind vectors which have been plotted on the images range in the interval* $[0, 10]\ m.s.^{-1}$*. Retrieved vertical wind maps on the highest layer lower boundary have been superimposed on the pressure difference images with a shaded red color for ascendant motion and a shaded blue color for descendant motion. Vertical wind ranges in the interval* $[-0.5, 0.5] m.s.^{-1}$ *.*

4 3D Visualization

We developed a dedicated interface to visualize our results in three dimensions. It is based on OpenGL and uses our software AMILab [1].

We define a rectangular region of interest (ROI) where we want to visualize our results in 3D. We distinguish three layers of clouds depending on their heights: low, medium and high. Those layers are directly obtained from an image of classification given by EUMETSAT.

Our 3D representation maps the image pixels to spherical coordinates of around the earth and the corresponding altitude. First, for each cloud layer, we compute the height s^k of the top of the clouds based on their temperature T given by the Eumetsat consortium as an input channel, using $s^k = \frac{T(s^k) - T_0}{\gamma}$, where $T_0 = 288.15\ K$ ($15^o C$) is the approximate temperature at sea level, and $\gamma = -6.510^{-3} K.m^{-3}$ is the standard constant lapse rate. In order to enhance the height visualization, a scaling factor of 25 is applied to the estimated height values.

We extrapolate the height s^k of each **cloud layer** h^k to the whole ROI using an iterative procedure based on two steps: a Gaussian smoothing step and a data attachment step that sets back the height of the clouds to their original values, for the pixels belonging to the corresponding layer. This procedure is applied 20 times with three different values of the Gaussian standard deviation: 10, 5, and 2 pixels successively, leading to a smooth mesh over the whole ROI. Each layer h^k can be visualized as a closed surface that

[1] `http://serdis.dis.ulpgc.es/~krissian/HomePage/Software/AMILab/`

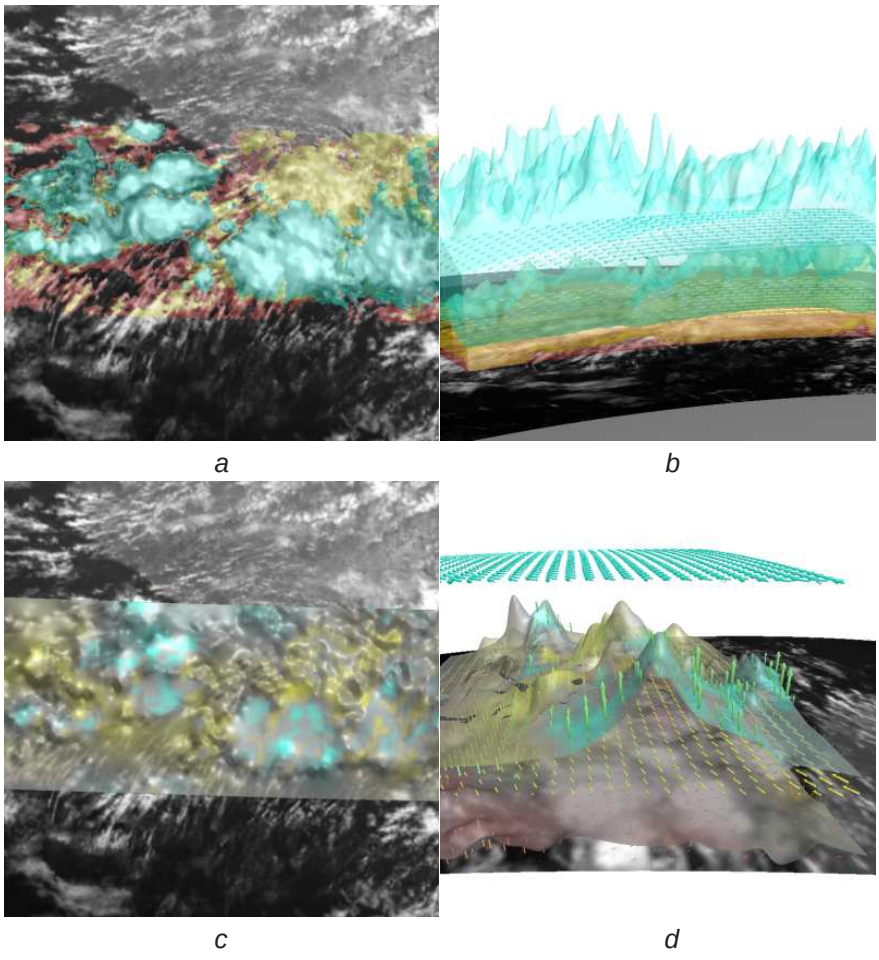

Figure 3: ***Visualization of 3D winds in atmospheric convective systems.*** ***a)*** *Top view of the three classes* (C^1, C^2, C^3) *of layers (over the Gulf Guinea at t=0 min).* ***b)*** *Depth view of layers* (h^1, h^2, h^3) *and winds* (v^1, v^2, v^3)*.* ***c)****Top view of the vertical wind field* w^3 *displaying ascendant winds (in blue) and descendant winds (in yellow).* ***d)*** *Depth view in perspective of wind fields* $(v^1, w^2, v^2, w^3, v^3)$ *and of layers* (h^1, h^2)*.*

covers the volume between the height of the top and bottom bounding surfaces (s^k, s^{k+1}). Each closed surface is displayed in a plain color, respectively red, yellow and cyan for the lower, intermediate and higher cloud layers (Fig. 3 *a* and *b*). Alternatively, the surface representing the top of the clouds of a given layer can also be color-coded. In this case, we only visualize the top of the clouds of the lower and intermediate layers as open surfaces. The meshes are color-coded depending on the estimated vertical winds w^k with colors ranging from the color of the given layer for descendant clouds to grey for clouds without vertical displacement, to the color of the direct higher layer for ascendant clouds. The mesh is also visualized with transparency as illustrated in Fig.3 *c* and *d*.

The horizontal v^k and the vertical w^k **winds** are represented by 3D arrows made of a circular cylindrical base and a cone for the head. The scaling and the spacing between successive arrows in X or Y directions can be set by interface. A typical value for the spacing is 10 pixels in each direction with a scaling of 5. Horizontal winds v^k are drawn at the average height $(s^{k+1} - s^k)/2$ while vertical winds w^k at the interface of two layers are represented on surfaces s^k. The color of the vertical vectors between two layers is an average color of the two layers. Fig.3 *b* and *d* illustrates the visualization of the calculated winds. The interface allows changing easily any of the parameters used for the visualization, and also permits real-time transformation like translation, zoom, and rotation of the scene. Thus, we believe that it can be helpful for an expert for comparing its understanding of a meteorological phenomenon with the results of our algorithm.

5 Experiments

We have performed a qualitative evaluations on a METEOSAT Second Generation meteorological sequence of 4 images acquired at a rate of an image every 15 minutes, with a spatial resolution of 3 kilometers at the center of the whole Earth image disk. The images of 512 by 200 pixels cover an area over the Gulf Guinea. The images are EUMETSAT top of cloud pressure observations which are associated to top of cloud classifications [9]. According to section 3.3, pressure images and classifications maps have been used to derive pressure difference image segments for 3 broad layers, at low, intermediate and high altitude. Figure 3 displays the pressure difference images related to the higher layer, together with the 3D estimated wind fields. One can visualize here large convective systems. They are characterized by strong ascendant flows which are smoothly reversed after bursting while reaching the tropopause cover. Such scenarios have been correctly estimated as shown in figure 3. Furthermore, let us remark that the time-consistency and the correct range wind values estimated of the retrieved 3D winds is a testimony of the stability of the estimation method.

6 Conclusions

In this paper, we have first presented a motion estimation method solving for the first time the complex problem of 3D winds field recovery from satellite image sequences. The estimator is based on a functional minimization. The data term relies on the 3D-ICE model which describes the dynamics of an interacting stack of atmospheric layers. The 3D-ICE model applies on a set of sparse pressure difference images related to the different atmospheric layers. A method is proposed to reconstruct such observations from satellite top of cloud pressure images and classification maps. To overcome the problem of sparse observations, a robust estimator is introduced in the data term. The data term is combined to a regularizers preserving bi-dimensional divergent and vorticity structures of the three-dimensional flow and enforcing regions of homogeneous vertical winds. We have then described a 3D visualization tool representing three different cloud layers, their correspoding heights, the horizontal winds within each layer and the vertical winds between two successive layers. We believe that this tool, allowing real-time visualization and interaction, is useful in understanding our results. The evaluation performed on METEOSAT pressure image sequences demonstrate the efficiency of the estimation method and the visualization capabilities.

References

[1] M. Black and P. Anandan. The robust estimation of multiple motions: Parametric and piecewise-smooth flow fields. *Comput. Vis. and Image Understanding*, 63(1):75–104, 1996.

[2] T. Corpetti, E. Mémin, and P. Pérez. Dense estimation of fluid flows. *IEEE Trans. Pat. Anal. Mach. Intell.*, 24(3):365–380, 2002.

[3] J.M. Fitzpatrick. The existence of geometrical density-image transformations corresponding to object motion. *Comput. Vision, Graphics, Image Proc.*, 44(2):155–174, Nov. 1988.

[4] P. Holland and R. Welsch. Robust regression using iteratively reweighted least-squares. *Commun. Statis.-Theor. Meth.*, A6(9):813–827, 1977.

[5] J.R. Holton. *An introduction to dynamic meteorology*. Academic press, 1992.

[6] B. Horn and B. Schunck. Determining optical flow. *Artificial Intelligence*, 17:185–203, 1981.

[7] R. Larsen, K. Conradsen, and B.K. Ersboll. Estimation of dense image flow fields in fluids. *IEEE trans. on Geosc. and Remote sensing*, 36(1):256–264, Jan. 1998.

[8] J.A. Leese, C.S. Novack, and B.B. Clark. An automated technique for obtained cloud motion from geosynchronous satellite data using cross correlation. *Journal of applied meteorology*, 10:118–132, 1971.

[9] H.J. Lutz. Cloud processing for meteosat second generation. Technical report, European Organisation for the Exploitation of Meteorological Satellites (EUMETSAT), Available at : http://www.eumetsat.de, 1999.

[10] D. Suter. Motion estimation and vector splines. In *Proc. Conf. Comp. Vision Pattern Rec.*, pages 939–942, Seattle, USA, June 1994.